

# Automatic Detection of *Aedes aegypti* Breeding Grounds Based on Deep Networks with Spatio-Temporal Consistency

Wesley L. Passos<sup>1</sup>, Gabriel M. Araujo<sup>2</sup>, Amaro A. de Lima<sup>2</sup>, Sergio L. Netto<sup>1</sup>, and Eduardo A. B. da Silva<sup>1</sup>.

**Abstract**—Every year, the *Aedes aegypti* mosquito infects millions of people with diseases such as dengue, zika, chikungunya, and urban yellow fever. The main form to combat these diseases is to avoid mosquito reproduction by searching for and eliminating the potential mosquito breeding grounds. In this work, we introduce a comprehensive dataset of aerial videos, acquired with an unmanned aerial vehicle, containing possible mosquito breeding sites. All frames of the video dataset were manually annotated with bounding boxes identifying all objects of interest. This dataset was employed to develop an automatic detection system of such objects based on deep convolutional networks. We propose the exploitation of the temporal information contained in the videos by the incorporation, in the object detection pipeline, of a spatio-temporal consistency module that can register the detected objects, minimizing most false-positive and false-negative occurrences. Using the ResNet-50-FPN as a backbone, we achieve F<sub>1</sub>-scores of 0.65 and 0.77 on the object-level detection of ‘tires’ and ‘water tanks’, respectively, illustrating the system capabilities to properly locate potential mosquito breeding objects.

**Index Terms**—vector control, *Aedes aegypti*, aerial images, convolutional neural networks, image and video processing, computer vision, object detection.

## I. INTRODUCTION

The mosquito *Aedes aegypti* is the transmitter of arboviral diseases such as dengue, zika, chikungunya, and urban yellow fever [1]. According to the World Health Organization, from 50 to 100 million dengue infections occur worldwide every year. In 2020, the Americas alone reported more than 2.3 million cases of dengue, most of them in Brazil [2]. Zika virus infection during pregnancy correlates to microcephaly and other congenital malformation; children in these conditions rarely develop normally [3]. It is estimated that there are 200,000 clinical cases of yellow fever, causing 30,000 deaths in the world yearly [4]. These diseases also have a strong economical impact. A survey conducted in 17 countries in the Latin and Central Americas estimates that the cost of dengue epidemics in these countries exceeds US\$ 3 billions annually, US\$ 1.4 billion only in Brazil [5]. These facts make the arboviruses transmitted by the *Aedes aegypti* one of the leading global health problems.

Except for the yellow fever, there are no vaccines nor specific antiviral drugs for the diseases transmitted by the *Aedes aegypti*. Thus, the current best form to combat these

diseases is still through the control and elimination of possible mosquito foci [6]. In fact, the impact of vector reduction on diseases spread has been a subject of study for a long time [7]. The *Aedes aegypti* reproduces in clean and stagnant water. So, any containers that store water (water tanks, buckets, ornamental fountains, plant dishes, water canisters for animals, tires, and others) are potential breeding grounds. Such objects are very common and can be found everywhere, which can make monitoring and controlling the mosquito, in the absence of proper technical support, expensive, time-consuming, and inefficient. Allying the knowledge of an expert with a tool that accelerates the search for potential mosquito foci can be very valuable in such scenario. Currently, organizations have been using unmanned aerial vehicles (UAVs) to inspect hard-to-reach sites [8]. However, usually, an expert has to perform a visual inspection to identify possible objects associated to the mosquito reproduction. This procedure tends to be time-consuming, tiresome, and, consequently, prone to failure.

In this work, we propose the use of images and videos captured by a UAV, also known as *drone*, to support local health agents in locating potential hazardous sites. We then describe a system to automate the analysis process by applying machine learning and computer vision techniques to aid the specialist in the localization of relevant mosquito foci. For this purpose, we present an annotated video database acquired by a UAV flying at different altitudes and following predetermined serpentine-like trajectories. In addition, using this database, we develop a system capable of detecting these potential productive breeding sites by inputting all video frames to the Faster R-CNN architecture [9]. We also propose a spatial-temporal consistency module that exploits the correlation of the information present in neighboring video frames by employing the phase correlation technique [10] to estimate the displacements of the detected objects from frame to frame. Using these displacements we perform motion compensation to register the object along the video, eliminating a good portion of false-positive and false-negative detections.

A study [11] shows that focusing on the most productive breeding sites, such as tires and water tanks, is almost as effective as targeting all possible object classes that are potential mosquito breeding grounds, with the advantage of optimizing time- and cost-related resources. Based on this fact, the focus of this work is on the detection of tires and water tanks.

In order to describe our contributions, this paper is organized as follows: Section II describes related works in the subject, whereas Section III describes the newly acquired

<sup>1</sup>Electrical Engineering Program (PEE/COPPE), Federal University of Rio de Janeiro (UFRJ), PO Box 68504, Rio de Janeiro, RJ, 21945-970, Brazil.

<sup>2</sup>Federal Center for Technological Education Celso Suckow da Fonseca (CEFET/RJ), Nova Iguaçu, RJ, 26041-271, Brazil. E-mails: {wesley.passos, sergioln, eduardo}@smt.ufrj.br. {gabriel.araujo, amaro.lima}@cefet-rj.br.

database. The proposed object-detection system is presented in Section IV, where we detail the proposed spatio-temporal consistency module that mitigates most incorrect and missed detections. Section V describes the experimental methodology employed to evaluate the proposed system in terms of its performance in detecting the objects of interest, and Section VI presents the obtained experimental results. Finally, Section VII concludes the paper by emphasizing its main technical achievements.

## II. RELATED WORK

In [12], the authors propose a system to identify potential mosquito breeding sites in geotagged images received from the population. The images are converted into feature vectors using the bag of visual words model through the scale-invariant feature transform (SIFT) descriptor to train a support vector machine (SVM) classifier. According to classification, the system outputs a heat map highlighting the regions with the highest risk of having mosquito habitats. The work in [13] uses an ensemble of naive Bayes classifiers with speeded-up robust features (SURF) extracted from thermal and gray level images to detect stagnant water. The approaches in [12], [13] only classify the images as to whether containing or not potential breeding grounds, not providing a precise spatial localization, basing the analysis on a limited number of object types.

The authors of [14] use images from Google Street View, Google image search, and Common Objects in Context (COCO) dataset to train and test the Faster R-CNN to detect tires, buckets, potted plants, garbage bins, vases, bowls, and cups. They use the detected objects to compose a dashboard showing the risk areas. In a test set, that system obtained a 0.91 performance in terms of  $F_1$ -score. Despite having promising results, due to the dataset characteristics, the method is only applicable to public places, *e.g.*, streets and avenues. Building on top of the system in [14], the authors of [15] designed an immersive visualization tool using a tiled-display wall, aimed at helping researchers and health agents to explore the datasets.

Aerial images can reveal mosquito breeding grounds in abandoned private or difficult to access areas. The papers in [16], [17] introduced a dataset to enable the design of this type of application. The work in [17] also proposed a method using optical flow and histograms in the hue, saturation, and value (HSV) color space as feature extractors and random forests to classify tires and stagnant water. Although the obtained results were promising, the dataset used was small and had little variability.

The work in [18] investigates how a UAV would compare to ground-truth GPS technology for mapping over a small geographical area and identifying relatively small artificial containers, such as bottles, cups, bags, and others, in terms of time, cost, and accuracy. In their study, nine external volunteers collected 678 waypoints data and 214 aerial images from commercial GPS receivers and a UAV, respectively, in an isolated parking lot. The authors observed that the UAV method was not as efficient as the GPS method for identifying small objects, as the GPS method achieved an  $F_1$ -score of 0.86 against 0.30 for the UAV method.

The works in [19] and [20] employed UAVs to detect water bodies that can be breeding sites for *Nyssorhynchus darlingi* or *Culex pipiens L.*, respectively. Both works used multispectral and RGB imagery to construct a georeferenced orthomosaic. The former [19] composed an eight-band orthomosaic and used a random forest algorithm to classify water bodies in the Amazon region with a high chance of having *Nyssorhynchus darlingi* in its aquatic stages. The latter [20] discriminated between tidal marsh water bodies based on their brightness in the multispectral orthomosaic. However, the cost and complexity associated with the use of multispectral images limit the applicability of the method.

The recent work in [21] addresses the detection of potential mosquito breeding grounds using a UAV by targeting water tanks as well as scenarios containing objects that can hold stagnant water. To conduct the study, the authors compose four datasets, namely DS1, DS2, DS3, and DS4, which are available upon request to the authors. Datasets DS1 and DS2 contain images with seven types of water tanks acquired from different altitudes (50 m and 70 m, respectively) and were used to build and evaluate a YOLOv3 model to detect this object type. Datasets DS3 and DS4 contain real and simulated scenarios, respectively, acquired with a manually-operated UAV, which can be classified as critical or normal, depending on the number of objects of interest present in the scene.

In the present work, we extend the dataset initially proposed in [16] by adding more videos and many more occurrences of the objects of interest. It also has additional variations regarding recording location, altitude, and object arrangements. The object annotation associated with the videos is dense, that is, it has been performed in all video frames. We also employ a Faster region-based convolutional neural network (Faster R-CNN) [9] at frame level to detect the objects of interest present in each frame. Another contribution of this work is the enhancement of the object detection by the exploitation of the temporal redundancy among the neighboring video frames. It is done so by employing a tracking method to mitigate detection inconsistencies. The phase correlation global motion estimation algorithm [10] is applied in successive frames to align them spatially in a time window. By doing so, we are able to incorporate a spatio-temporal consistency analysis that combines different detections in different frames of the same object, thus greatly reducing the numbers of false and missing detections.

## III. MBG VIDEO DATABASE

A proper database for detecting and classifying objects in aerial videos should have: (i) control of the maximum number of recording parameters; (ii) an expressive number of samples for each object class; (iii) variability of the background, object position, luminosity, and height; (iv) no camera distortions; and, last but by no means least, (v) reliable object annotation (position and classification).

In this sense, we present an annotated video database devised for detecting mosquito breeding grounds (MBG) in aerial videos. Drone telemetry (altitude, latitude, longitude,

and flying speed) is also available, allowing geolocalization of all objects of interest identified by their corresponding bounding boxes. We use the commercial Phantom Vision 4 PRO UAV from DJI Company [22] for acquiring the aerial videos using a high-definition camera with passive and active stabilization (dampers and gimbal).

The so-called MBG database has the following technical specifications:

- The drone performs a preprogrammed serpentine-like sweep over the entire terrain area autonomously, without any human intervention during video acquisition. Such operating mode allows for greater reproducibility and uniformity of recording patterns, which becomes independent from the UAV pilot.
- Camera auto adjustment is turned off and its parameters are set manually, in order to guarantee uniformity and total control over the recording process. In that manner, camera focus is fixed at infinity and the video scan is performed at  $3840 \times 2160$  or  $4096 \times 2160$  resolutions at 24 frames per second (fps).
- Before each flight, a calibration video is recorded using a chessboard pattern to allow compensation for major lens distortions using Zhang's method [23].
- The altitude is set to be constant for the whole duration of any video. Currently, the database has videos acquired at different altitudes, e.g., 10, 25, 40 m, all of them predefined in the flight plan. Small variations in altitude ( $\pm 0.5$  m, according to the manufacturer [22]) caused by the limited accuracy of telemetry, wind, etc., are within acceptable ranges. Such a height range lends the database a wide applicability: the higher altitudes enable a large area sweep during a single video take, while the small altitudes enable the identification of small objects such as 'tires' and 'bottles'.
- Speed approximately constant of 15 km/h is preset in the flying plan, with possible small variations caused by wind, for example.
- The dataset includes different types of scenes, such as grass, street, buildings, empty lots, and urban areas.
- All videos are manually annotated in a frame-by-frame manner using the CVAT software [24].

The MBG database is publicly available at [25]. It is presently composed of 13 video sequences acquired by a drone platform recorded in 11 different locations, as detailed in Table I. Three of these locations are actual urban areas, while the others had the objects of interest manually inserted into the scene in random positions before recording the videos. Some examples of screenshots of three different MBG videos are shown in Fig. 1, whereas Fig. 2 illustrates examples of objects of interest present in the recorded scenes.

The MBG database contains 79,562 frames with a total of 88,281 annotated bounding boxes, comprising several objects such as 'bottles', 'buckets', 'pools', 'puddles', 'tires', and 'water tanks'. The large number of annotated bounding boxes enables one to train object detectors employing deeper networks, which require large amounts of data for proper parameter adjustment. Table II shows, for each MBG video

sequence, the amount of objects of each type and their corresponding number of annotated bounding boxes.

The annotation files are provided in XML format for video tasks as provided by CVAT [24]. The XML file contains tracks, and each track corresponds to an object which can be presented on multiple frames. Yet, the objects 'bucket', 'poll', and 'water tank' have attributes to indicate object material (plastic or asbestos in 'water tank' case), whether it is open or not ('water tank' case), or if it contains water ('pool' and 'bucket' cases).

## IV. SYSTEM DEVELOPMENT

### A. Object detection

Object detection is a classic task in computer vision that consists of both locating and classifying one or more instances of objects in images or videos. The detector assigns a set of bounding boxes to each image, containing their coordinates, labels, and confidence scores.

The so-called faster region-based convolutional neural network (Faster R-CNN) [9] is a CNN-based meta-architecture that showed excellent results in various applications and object-detection competitions [26]. The Faster R-CNN, as illustrated in Fig. 3, is basically composed of a feature extractor, a region proposal generator (or region proposal network, RPN), together with a classification and regression (cls/reg) module. In the present work, feature maps are extracted from the input images by using a ResNet-50 convolutional network [27] with feature pyramid networks (FPN) [28]. Based on these maps, the RPN generates potential regions of interest (RoI), which are delivered to the cls/reg module. This module is composed of densely connected layers that identify the precise RoI boundaries and content classes along with their estimated probabilities. In this work, these probabilities are referred to as confidence scores; commonly, they are used to characterize a detection in the sense that it is considered positive only if its confidence is larger than a threshold  $\tau$ . The detections whose confidence level is less than  $\tau$  are discarded. The confidence threshold  $\tau$  is a parameter that is usually set during the system training/validation procedure.

### B. Spatio-temporal tube for object registration

When dealing with videos, standard object-detection models do not intrinsically consider the temporal dimension, i.e., each detection of the same object is treated independently across distinct frames. If, however, one is concerned with whether an object is present in the scene recorded as the whole set of video frames, as is the case in our application, a post-processing stage is required to combine the bounding boxes of the same object in different frames. The works in [29], [30], [31], [32] attempt to combine the detection outputs in several frames to make the object detection results more coherent and stable. The authors of [29] attempt to match overlapping detections across frames within the video sequence according to their IOU, without any motion compensation. The work in [30] employs context information from two different object detection models and optical flow to suppress false positives and propagate detections across frames to reduce false negatives. As it combines the output of two different object detection

Table I: Summary of characteristics of each video in the MBG database. The heights are given in meters, the video durations in minutes and the video resolutions are given by the width of the frames in pixels.

Video #	Scene composition	Height [m]	Duration [min]	Resolution [pixels]
01	low grass	10	02:32	3840
02	low grass and street	15	00:23	3840
03	low grass, street and buildings	40	03:44	3840
04	low grass and street	15	02:06	3840
05	empty lot	10	00:41	3840
06	empty lot	16	01:15	3840
07	empty lot	20	03:07	3840
08	grass	10	01:37	3840
09	buildings	40	02:41	3840
10	urban zone	40	05:27	4096
11	urban zone	40	05:27	4096
12	urban zone	40	04:33	4096
13	urban zone	40	03:30	4096



Figure 1: Selected frames of video sequences from the MBG database, showing annotated bounding boxes.

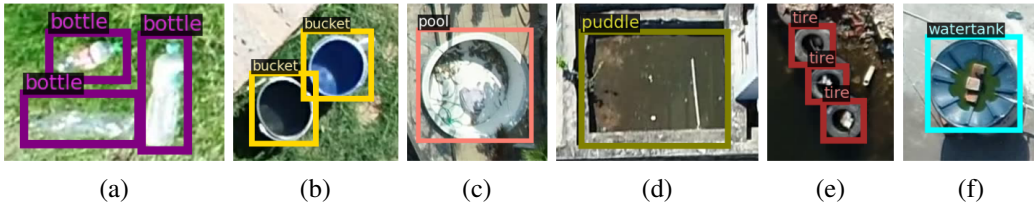


Figure 2: Examples of objects associated to potential mosquito breeding grounds in the MBG database: (a) ‘bottle’, (b) ‘bucket’, (c) ‘pool’, (d) ‘puddle’, (e) ‘tire’, and (f) ‘water tank’.

models, it seems to be computationally complex. The authors of [31] associate overlapping bounding boxes from adjacent pairs of frames to create and re-score object instances and uses them to infer missed detections. That approach interpolates consecutive frame contents assuming a linear object movement, which may lead to wrong detections. The work in [32] proposes a learning-based association method for bounding

boxes, which does not rely on IOU, and requires specific data for its training.

In the present work, we consider the presence of an object in the scene as a whole by looking at the entire collection of video frames. We do so in a simple yet effective way, by introducing, in the object detection pipeline, the spatio-temporal tube (STT) concept [33], that integrates spatial and temporal localization



Table II: Number of annotated object types per MBG video (labeled as ‘unique’), together with their corresponding number of annotated bounding boxes.

Video #	bottle		bucket		pool		puddle		tire		water tank	
	unique	bboxes	unique	bboxes	unique	bboxes	unique	bboxes	unique	bboxes	unique	bboxes
01	9	474	2	91	1	53	0	0	6	271	0	0
02	7	485	2	135	1	75	0	0	6	397	0	0
03	0	0	1	161	0	0	0	0	0	0	25	3083
04	9	283	3	101	3	103	0	0	7	339	0	0
05	8	356	4	192	4	171	0	0	10	447	0	0
06	1	71	6	405	5	360	0	0	6	456	1	70
07	7	605	4	452	3	265	1	86	7	605	0	0
08	11	666	1	214	1	38	0	0	6	261	0	0
09	0	0	3	281	1	99	2	145	2	192	39	2995
10	6	467	26	2397	5	424	0	0	49	4390	312	25967
11	3	285	10	972	8	839	0	0	27	2625	332	30855
12	0	0	2	342	2	339	0	0	7	1278	3	383
13	2	162	2	182	2	185	0	0	7	706	0	0
<b>Total</b>	<b>63</b>	<b>3854</b>	<b>66</b>	<b>5925</b>	<b>36</b>	<b>2951</b>	<b>3</b>	<b>231</b>	<b>140</b>	<b>11967</b>	<b>712</b>	<b>63353</b>

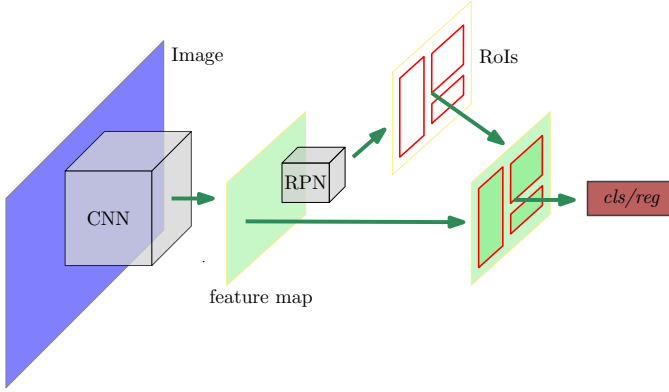


Figure 3: Block diagram for the Faster R-CNN architecture. In this scheme, the CNN extracts convolutional feature maps from the input images and the RPN generates potential RoIs. These RoIs are then classified and refined by the classification and regression (cls/reg) module.

of the same object. The STT can be viewed as an extension of the 2D spatial bounding boxes present in isolated frames to 3D spatio-temporal bounding boxes defined in a 3D space induced by a set of neighboring video frames. More precisely, an STT  $T_o$  of an object  $o$  is the spatio-temporal region defined as the concatenation of the bounding boxes associated with this object in every frame of a video, that is,

$$T_o = [B_{o,q} B_{o,q+1} \cdots B_{o,q+r}], \quad (1)$$

where  $B_{o,k}$  is the bounding box of the object  $o$  in frame  $k$  of a video that comprises  $Q$  consecutive frames indexed by  $k = q, q+1, \dots, (q+Q-1)$ .

The main challenge in the STT approach is how to associate different model outputs with a particular STT. In this work, we propose a methodology designed taking into account the peculiarities of the MBG database: (i)

- 1) Displacement between adjacent frames is mainly translational;

- 2) STT sections in a time interval have the same orientation in 3D space-time, which implies that, although STTs may intersect, they cannot cross each other; and
- 3) STTs are continuous, which is derived from the fact that a given object cannot appear, disappear, and reappear in consecutive frames.

With these points in mind, an algorithm to compose the STTs can be implemented according to the following steps: I.

- 1) The object spatial displacement between two consecutive frames is estimated by a global motion estimation algorithm such as the phase-correlation [10]. Global motion estimation algorithms are good choices in this case because one can safely assume that, for the objects of interest (see Figure 2), parallax effects are negligible at the drone heights in which the videos of the MBG database have been acquired (see Table I).
- 2) The computed displacement is employed to estimate the spatial position of the objects across different frames and, as a result, one can associate each bounding box to a particular STT.
- 3) Having aligned the frames spatially, we compute the pairwise intersection of union (IOU) of the detected bounding boxes in two consecutive frames. We consider that the bounding boxes from two consecutive frames belong to the same STT  $T_n$  and, consequently, to the same object, if the IOU between these two bounding boxes is maximum and greater than 0.5. More precisely, given frames  $q$  and  $q+1$  aligned by global motion estimation, bounding boxes  $B_{n,q}$  and  $B_{n,q+1}$ , in frames  $q$  and  $q+1$ , respectively, are associated to the same STT  $T_n$  if the following condition holds:

$$\text{IOU}(B_{m,q+1}, B_{n,q}) \geq \text{IOU}(B_{o,q+1}, B_{n,q}) \geq 0.5, \quad \forall o. \quad (2)$$

If this condition does not hold, we may have either a missed (false negative) or an incorrect (false positive) detection, which can be discarded altogether.

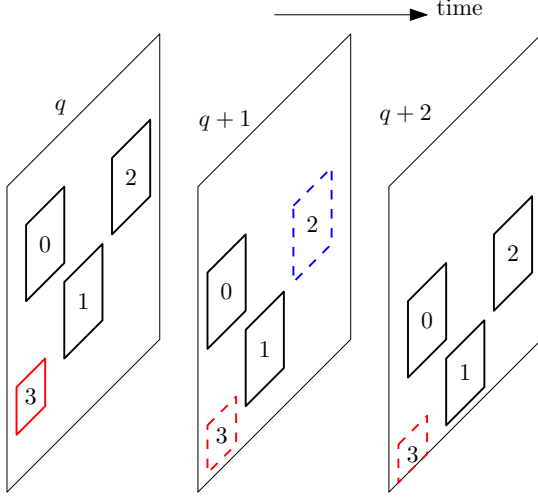


Figure 4: Example of bounding box associations to constitute spatio-temporal tubes (STTs). Solid black lines are detections (model output) over these frames and dashed lines are projected detections from a previous frame. The collection of detections and/or estimates having the same object identity form an STT.

To illustrate the procedure, let us consider the example depicted in Fig. 4, where the rectangles with the same number are detections of the same object in different frames (bounding boxes with  $\max(\text{IOU}) \geq 0.5$  among aligned frames). In this sense, object 2 characterizes a false negative (dashed-blue bounding box) in frame  $q + 1$ , while object 3 characterizes a false positive (solid-red bounding box) in frame  $q$ . The idea is to identify the detections associated with the same object along the whole video, as depicted in Fig. 5, where the object spatio-temporal localization in the video is represented by the pink path.

Let  $l_i$  be the number of detections output by the model within  $\text{STT}_i$ , and let  $m_i$  be the number of frames comprising  $\text{STT}_i$ , that is, the number of frames contained in the interval between the first frame and the last frame in which the object that is associated with  $\text{STT}_i$  is detected. In order to evaluate if a given  $\text{STT}_i$  is associated to an actual object of interest, we test  $(l_i/m_i)$  against a consistency threshold  $\mu$ . If  $(l_i/m_i) \geq \mu$ , then  $\text{STT}_i$  is equivalent to a detected object. The STT consistency threshold  $\mu$  is a parameter to be tuned in the system training/validation process.

## V. EXPERIMENTAL METHODOLOGY

### A. Performance evaluation

To evaluate the network detections it is necessary to establish an IOU threshold  $t$ , which will determine each detection as correct (true positive, TP) or incorrect (false positive, FP). One metric widely used in the context of object detection is the average precision with  $\text{IOU} \geq 0.5$  ( $\text{AP}_{50}$ ) [33], that is, TPs and FPs are defined with  $t = 0.5$ . The AP metric aggregates the compromise between TPs and FPs for all confidence thresholds  $\tau$ . In the application associated with this work, that is the detection of mosquitoes breeding grounds, it is

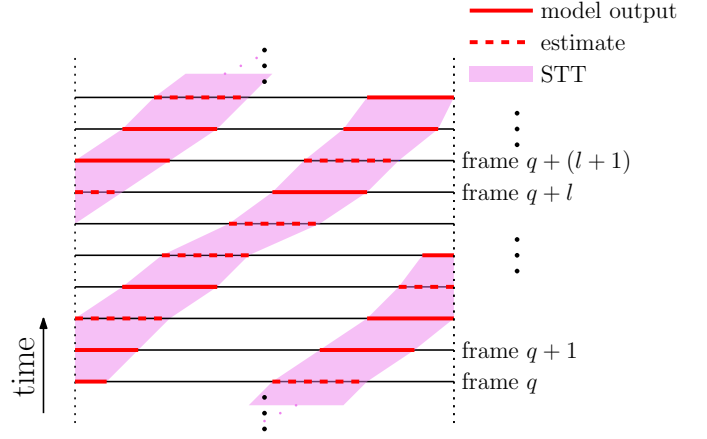


Figure 5: STT representation (pink spatio-temporal regions) across consecutive video frames (indicated by black solid lines). Solid red lines are detections (model output) over these frames and dashed red lines are projected detections from a previous frame. The collection of detections and/or estimates having the same object identity form a given STT.

also useful to report particular values of TP, FP, and missed (false negative, FN) detections. In addition, to aggregate the TP, FP, and FN information, we also report precision (Pr), recall (Rc), and  $F_1$ -score. Since one considers as positives only those detections whose confidence is larger than a confidence threshold  $\tau$ , these can be expressed as [33]:

$$\text{Pr}(\tau) = \frac{\sum_{n=1}^S \text{TP}_n(\tau)}{\sum_{n=1}^S \text{TP}_n(\tau) + \sum_{n=1}^{N-S} \text{FP}_n(\tau)}, \quad (3)$$

$$\text{Rc}(\tau) = \frac{\sum_{n=1}^S \text{TP}_n(\tau)}{\sum_{n=1}^S \text{TP}_n(\tau) + \sum_{n=1}^{G-S} \text{FN}_n(\tau)}, \quad (4)$$

$$F_1(\tau) = 2 \frac{\text{Pr}(\tau) \text{Rc}(\tau)}{\text{Pr}(\tau) + \text{Rc}(\tau)}, \quad (5)$$

where  $G$  is the number of ground-truths in the dataset and  $N$  is the number detections output by the model, of which  $S$  are correct ( $S \leq G$ ).

The aforementioned metrics evaluate the system performance at a bounding-box level. However, as discussed in Subsection IV-B, when dealing with videos, one may be mostly interested in evaluating the system performance at the object level, using STTs. In this case, one can use the STT-AP metric, proposed in [33], which is computed in a way equivalent to the one in which the AP metric is computed, with the difference that the bounding boxes are replaced by STTs. In that manner, an object is considered a TP if the STT-IOU is equal or greater than a chosen threshold  $t_T$ , which was set to  $t_T = 0.5$  in this work, yielding the metric that we refer to as  $\text{STT-AP}_{50}$ .

Likewise the case of the AP metric, in the STT-AP all the model predictions are ranked for each class according to the predicted confidence level  $\tau$  (from the highest to the lowest), irrespective of their correctness. The confidence level  $\tau_T$  assumed for an STT is the average confidence of the bounding boxes corresponding to each of its constituent frames. The all-point interpolation [33] may be then performed in order to compute the final STT-AP value. We also report the TP, FP and FN as well as the Pr, Rc and  $F_1$  at STT level, which can be computed using Eqs. (3), (4), and (5) by using both  $\tau$  and  $\mu$  as thresholds.

### B. Training the Faster R-CNN

For the sake of development of the proposed mosquito breeding grounds detection system, the MBG database was initially split into training and test sets. The five videos exclusively assigned to the test set (01, 02, 05, 09, and 13) are only used for final model evaluation. Targeting model development and hyper-parameter tuning, a leave-one-out cross-validation scheme [34] was employed. In this procedure, the training set was partitioned in eight folds, as shown in Table III, where seven videos were used for the actual training and the remaining one was used for validation.

Table III: Training and validation sets used in the experiments with the MBG dataset. Videos 01, 02, 05, 09, and 13 were exclusively assigned to the test set.

Fold	Video #	
	Training	Validation
1	04, 06, 07, 08, 10, 11, 12	03
2	03, 06, 07, 08, 10, 11, 12	04
3	03, 04, 07, 08, 10, 11, 12	06
4	03, 04, 06, 08, 10, 11, 12	07
5	03, 04, 06, 07, 10, 11, 12	08
6	03, 04, 06, 07, 08, 11, 12	10
7	03, 04, 06, 07, 08, 10, 12	11
8	03, 04, 06, 07, 08, 10, 11	12

All models are initialized with the public available weights [35] trained on the COCO database and are further trained in the MBG database with a learning rate of 0.002.

In the case the system was tuned with the frame-level metrics, having the eight best models in each training and validation fold, the confidence interval  $\tau$  of the Faster R-CNN was tuned by exhaustive search in the set from  $\tau = 0.1$  to  $\tau = 0.9$  in increments of 0.1 with the added confidence intervals  $\tau = 0.05$  and  $\tau = 0.99$ , according to the best  $F_1$  value averaged over all validation sets. The best confidence interval was found to be  $\tau = 0.99$  for both the ‘tire’ and ‘water tank’ cases.

For the final model, once the confidence threshold  $\tau$  was set, the system was retrained with all eight videos in the original training set. To mitigate overfitting, this final training process is interrupted at iteration  $I$ , which is the median value of the iteration indexes  $I_i$ , for  $i = 1, 2, \dots, 8$  that correspond to the minimum loss-function value in each validation run.

### C. Tuning the STT hyper-parameter

The procedure described in Section IV-B was applied to generate the STTs, aggregating the object-related temporal and spatial information present in the videos. In order to tune the model according to STT-based metrics, hyperparameters were searched for, namely the confidence threshold  $\tau$  of the Faster R-CNN and the consistency threshold  $\mu$  of the STT (see Subsection IV-B). After grid search, the confidence threshold was set to  $\tau = 0.99$ , and the model consistency threshold was set to  $\mu = 0.4$  for both ‘tire’ and ‘water tank’ object classes by maximizing the average  $F_1$ -score for the STTs across all eight validation folds.

## VI. EXPERIMENTAL RESULTS AND DISCUSSION

### A. Frame-level object detection

The frame-level performance of each of the eight Faster R-CNN trained models was evaluated in the test set, as given in Tables IV and V for the ‘tire’ and ‘water tank’ object classes, respectively, presenting satisfactory  $AP_{50}$  results in both cases.

Overall, the models were able to identify correctly the majority of the ‘tires’ in the MBG dataset presenting a very low number of FPs. The 16 FP occurrences in fold 8, a figure much larger than the ones of the other folds, are probably due to the validation video being a bit darker than the training ones. This hampered the network ability to distinguish between round shadows and tires. In addition, most of the FN figures correspond to tires that were placed at particularly challenging positions, as discussed in Subsection VI-B. In the case of ‘water tanks’, the models show satisfactory results in terms of  $F_1$ , which is a good compromise between Pr and Rc.

The last rows in Tables IV and V show the results for the final model obtained by training the Faster R-CNN using all eight available training videos. As one may observe, in this last row all resulting performance metrics are within the mean  $\pm$  std interval of the set of folds, indicating a stable and robust training procedure. Also, the final model performed better in the test set in terms of  $F_1$ , indicating that the network benefits from more data.

In the case of frame-level metrics, as the same object repeatedly appears along several frames, it contributes more than once for the TP, FP, and FN scores. This distortion is mitigated with the STT-level analysis, whose results are discussed in the following subsection.

### B. STT-level object detection

In this section, bounding boxes that correspond to the same object along consecutive frames are counted as a single tube, as detailed in Subsection IV-B, and all performance metrics are determined at the STT level. Tables VI and VII show the results for the object detection considering the video as a whole, using STTs. From these tables, one readily notices a drastic reduction in all FP values due to the temporal consistency imposed by the STT concept.

For the ‘tire’ object class, one may note the high TP scores and low FP values, leading to a high system precision. Some examples of correct ‘tire’ detections are depicted in

Table IV: Frame-level, bounding-box based results on the test set for object class ‘tire’, considering an IOU threshold  $t = 0.5$  and  $\tau = 0.99$ .

Fold	AP <sub>50</sub>	TP	FP	FN	Pr	Rc	F <sub>1</sub>
1	61.06	53	9	27	0.85	0.66	0.75
2	58.69	50	6	30	0.89	0.63	0.74
3	59.52	51	5	29	0.91	0.64	0.75
4	50.19	47	9	33	0.84	0.59	0.69
5	55.84	47	5	33	0.90	0.59	0.71
6	64.79	55	7	25	0.89	0.69	0.77
7	58.29	49	3	31	0.94	0.61	0.74
8	51.36	48	16	32	0.75	0.60	0.67
average	57.47	50.00	7.50	30.00	0.87	0.63	0.73
std	4.87	2.88	4.00	2.88	0.06	0.04	0.04
final	58.57	51	5	29	0.91	0.64	0.75

Table V: Bounding-box based results on the test set for object class ‘water tank’, considering an IOU threshold  $t = 0.5$  and  $\tau = 0.99$ .

Fold	AP <sub>50</sub>	TP	FP	FN	Pr	Rc	F <sub>1</sub>
1	64.12	102	48	25	0.68	0.80	0.74
2	66.85	103	39	24	0.73	0.81	0.77
3	70.16	108	50	19	0.68	0.85	0.76
4	65.60	108	54	19	0.67	0.85	0.75
5	65.15	105	44	22	0.70	0.83	0.76
6	58.03	101	63	26	0.62	0.80	0.69
7	67.33	109	62	18	0.64	0.86	0.73
8	70.16	109	50	18	0.69	0.86	0.76
average	65.93	105.63	51.25	21.38	0.67	0.83	0.74
std	3.87	3.29	8.26	3.29	0.04	0.03	0.02
final	65.46	105	44	22	0.70	0.83	0.76

Fig. 6, where one observes how the system is able to detect successfully tires of very different thicknesses. Most FN cases for the ‘tire’ class are associated with the target objects in the vertical position or stacked, thus causing partial occlusion, as illustrated in Fig. 6. Such cases are underrepresented in the training set. An interesting case of FP is also shown in Fig. 6 in which the trained model detected the tire that is part of the car.

In the ‘water tank’ class, the system is capable of retrieving 90% of the objects present in the test set, including several cases of different standards and colors, as illustrated in Fig. 7. Most FP occurrences in this class are due to objects that, even to the human eye, can be easily mistaken for ‘water tanks’, as also depicted in Fig. 7. In addition, most FN cases are related to the object being positioned in the shadow, occluded, or even upside-down. All these detection problems may be mitigated by possible database extension to incorporate more instances of these critical situations.

## VII. CONCLUSION

In this work, the automatic detection of *Aedes aegypti* mosquitoes foci using videos acquired with an autonomous UAV was addressed. A database of aerial images that contains several objects commonly associated with potential mosquito

Table VI: STT based test results on the test set for object class ‘tire’, considering an STT-IOU threshold  $t_T = 0.5$  and consistency threshold  $\mu = 0.4$ .

Fold	STT-AP <sub>50</sub>	TP	FP	FN	Pr	Rc	F <sub>1</sub>
1	58.21	18	1	13	0.95	0.58	0.72
2	61.24	19	1	12	0.95	0.61	0.75
3	54.46	17	0	14	1.00	0.55	0.71
4	51.49	16	3	15	0.84	0.52	0.64
5	51.16	16	2	15	0.89	0.52	0.65
6	60.59	19	3	12	0.86	0.61	0.72
7	54.29	17	1	14	0.94	0.55	0.69
8	53.97	17	2	14	0.89	0.55	0.68
average	55.67	17.38	1.63	13.63	0.92	0.56	0.69
std	3.89	1.19	1.06	1.19	0.05	0.04	0.04
final	51.48	16	2	15	0.89	0.52	0.65

Table VII: STT based test results on the test set for object class ‘water tank’, considering an STT-IOU threshold  $t_T = 0.5$  and consistency threshold  $\mu = 0.4$ .

Fold	STT-AP <sub>50</sub>	TP	FP	FN	Pr	Rc	F <sub>1</sub>
1	71.61	33	18	6	0.65	0.85	0.73
2	71.81	32	17	7	0.65	0.82	0.73
3	67.04	34	20	5	0.63	0.87	0.73
4	61.83	34	21	5	0.62	0.87	0.72
5	74.08	33	15	6	0.69	0.85	0.76
6	69.82	35	22	4	0.61	0.90	0.73
7	62.47	34	27	5	0.56	0.87	0.68
8	65.95	35	21	4	0.63	0.90	0.74
average	68.08	33.75	20.13	5.25	0.63	0.87	0.73
std	4.50	1.04	3.64	1.04	0.04	0.03	0.02
final	71.33	35	17	4	0.67	0.90	0.77

breeding grounds was introduced. A complete system for detecting objects of interest was proposed, working in two stages: first, object detection is performed frame-by-frame using the Faster R-CNN architecture; later, a subsequent step registers successive detections and imposes spatio-temporal consistency to the detection process which is performed at the object level. Using the ResNet-50-FPN as a backbone, it was possible to obtain an F<sub>1</sub>-score of 0.65 and 0.77 for the ‘tire’ and ‘water tank’ classes, respectively, which are considered the most critical objects for the *Aedes aegypti* wide reproduction. As can be inferred from our results, there is good evidence that the system can be improved with more training data. However, as discussed in this paper, acquiring and performing through bounding box annotation in such data is not an easy task. As a future direction, one may use active or self-learning to help in the annotation process of future acquired videos. Artificial data augmentation using generative adversarial neural networks could also lead to improved results.

## ACKNOWLEDGMENT

This study was financed in part by the Coordenação de Aperfeiçoamento de Pessoal de Nível Superior – Brasil (CAPES) – Finance Code 001; Fundação Carlos Chagas Filho de Amparo à Pesquisa do Estado do Rio de Janeiro (FAPERJ); Conselho Nacional de Desenvolvimento Científico



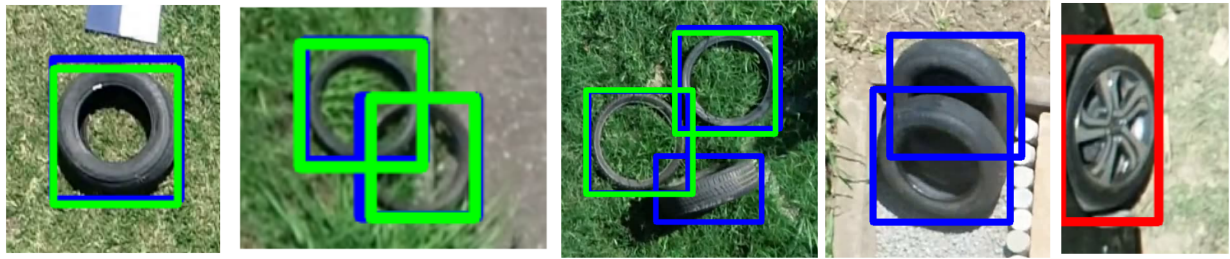


Figure 6: Example results of ‘tires’ detection, with some manual annotation (blue), correct detection (TP, in green), and false detection (FP, in red). Note that the blue boxes not overlaid by a green box are false negatives (FN).



Figure 7: Example results of ‘water tank’ detection, with some manual annotation (blue), correct detection (TP, in green), and false detection (FP, in red). Note that the blue boxes not overlaid by a green box are false negatives (FN).

e Tecnológico (CNPq); and Google Latin America Research Awards (LARA), 2019–2020 and 2020–2021. The authors would like to express their gratitude to the students from CEFET/RJ *campus* Nova Iguaçu whose work was fundamental to the database annotation process.

## REFERENCES

- [1] C. Rückert, J. Weger-Lucarelli, S. M. Garcia-Luna, M. C. Young, A. D. Byas, R. A. Murrieta, J. R. Fauver, and G. D. Ebel, “Impact of simultaneous exposure to arboviruses on infection and transmission by *Aedes aegypti* mosquitoes,” *Nature Communications*, vol. 8, pp. 1–9, May 2017.
- [2] Pan American Health Organization, “Reported Cases of Dengue Fever in The Americas,” <https://www3.paho.org/data/index.php/en/mnu-topics/indicadores-dengue-en/dengue-nacional-en/252-dengue-pais-ano-en.html>, 2021, accessed: 2021-08-27.
- [3] World Health Organization, “Zika virus,” <https://www.who.int/news-room/fact-sheets/detail/zika-virus>, 2018, accessed: 2021-08-27.
- [4] Pan American Health Organization, “Yellow Fever,” [https://www3.paho.org/hq/index.php?option=com\\_content&view=article&id=9476:yellow-fever&Itemid=40721&lang=en](https://www3.paho.org/hq/index.php?option=com_content&view=article&id=9476:yellow-fever&Itemid=40721&lang=en), 2019, accessed: 2021-08-27.
- [5] A. Laserna, J. Barahona-Correa, L. Baquero, C. Castañeda-Cardona, and D. Rosselli, “Economic impact of dengue fever in Latin America and the Caribbean: A systematic review,” *Revista Panamericana de Salud Pública*, vol. 42, p. e111, sep 2018.
- [6] L. Lambrechts and A. Failloux, “Vector biology prospects in dengue research,” *Memórias do Instituto Oswaldo Cruz*, vol. 107, no. 8, pp. 1080–1082, dec 2012.
- [7] J. B. Smith, “The logical basis of the sanitary policy of mosquito reduction,” *Science*, vol. 22, no. 570, pp. 689–699, Dec. 1905.
- [8] Prefeitura de Vitória, “Zika: Prefeitura usa drones no combate aos focos do mosquito,” <https://www.vitoria.es.gov.br/noticia/zika-prefeitura-usa-drones-no-combate-aos-focos-do-mosquito-19703>, 2015, accessed: 2021-09-02.
- [9] S. Ren, K. He, R. Girshick, and J. Sun, “Faster R-CNN: Towards real-time object detection with region proposal networks,” *IEEE Transactions on Pattern Analysis and Machine Intelligence*, vol. 39, no. 6, pp. 1137–1149, jun 2017.
- [10] B. S. Reddy and B. N. Chatterji, “An FFT-based technique for translation, rotation, and scale-invariant image registration,” *IEEE Transactions on Image Processing*, vol. 5, no. 8, pp. 1266–1271, 1996.
- [11] W. Tun-Lin, A. Lenhart, V. S. Nam, E. Rebollar-Téllez, A. C. Morrison, P. Barbazan, M. Cote, J. Midega, F. Sanchez, P. Manrique-Saide, A. Kroeger, M. B. Nathan, F. Meheus, and M. Petzold, “Reducing costs and operational constraints of dengue vector control by targeting productive breeding places: a multi-country non-inferiority cluster randomized trial,” *Tropical Medicine & International Health*, vol. 14, no. 9, pp. 1143–1153, Sep. 2009.
- [12] A. Agarwal, U. Chaudhuri, S. Chaudhuri, and G. Seetharaman, “Detection of potential mosquito breeding sites based on community sourced geotagged images,” in *Geospatial InfoFusion and Video Analytics IV; and Motion Imagery for ISR and Situational Awareness II*, Jul. 2014, p. 90890M.
- [13] M. Mehra, A. Bagri, X. Jiang, and J. Ortiz, “Image analysis for identifying mosquito breeding grounds,” in *IEEE International Conference on Sensing, Communication and Networking*, London, UK, Jun. 2016, pp. 1–6.
- [14] P. Haddawy, P. Wettayakorn, B. Nonthaleerak, M. S. Yin, A. Wirat-sudakul, J. Schöning, Y. Laosiritaworn, K. Balla, S. Euaungkanakul, P. Quengdaeng, K. Choknitipakin, S. Traivijitkhun, B. Erawan, and T. Kraissang, “Large scale detailed mapping of dengue vector breeding sites using street view images,” *PLOS Neglected Tropical Diseases*, vol. 13, no. 7, pp. 1–27, Jul. 2019.
- [15] M. Prachyabrued, P. Haddawy, K. Tengputtipong, M. S. Yin, D. Bicut, and Y. Laosiritaworn, “Immersive visualization of dengue vector breeding sites extracted from street view images,” in *IEEE International Conference on Artificial Intelligence and Virtual Reality*, Utrecht, Netherlands, Dec. 2020, pp. 37–42.
- [16] W. L. Passos, T. M. Dias, H. M. A. Junior, B. D. Barros, G. M. Araujo, A. A. Lima, E. A. B. da Silva, and S. L. Netto, “Acerca da detecção automática de focos do mosquito *Aedes aegypti*,” in *Brazilian Symposium on Telecommunications and Signal Processing*, Campina Grande, Brazil, Sep. 2018, pp. 392–396.
- [17] T. M. Dias, V. C. Alves, H. Alves, L. F. Pinheiro, R. S. G. Pontes, G. M. Araujo, A. A. Lima, and T. M. Prego, “Autonomous detection of mosquito-breeding habitats using an unmanned aerial vehicle,” in *2018 Latin American Robotic Symposium, 2018 Brazilian Symposium on Robotics and 2018 Workshop on Robotics in Education*, 2018, pp. 351–356.
- [18] J. Schenkel, P. Taele, D. Goldberg, J. Horney, and T. Hammond, “Identifying potential mosquito breeding grounds: Assessing the efficiency of UAV technology in public health,” *Robotics*, vol. 4, no. 9, p. 91, Nov. 2020.
- [19] G. Carrasco-Escobar, E. Manrique, J. Ruiz-Cabrejos, M. Saavedra,

- F. Alava, S. Bickersmith, C. Prussing, J. M. Vinetz, J. E. Conn, M. Moreno, and D. Gamboa, "High-accuracy detection of malaria vector larval habitats using drone-based multispectral imagery," *PLOS Neglected Tropical Diseases*, vol. 13, no. 1, pp. 1–24, Jan. 2019.
- [20] E. J. Haas-Stapleton, M. C. Barretto, E. B. Castillo, R. J. Clausnitzer, and R. L. Ferdan, "Assessing mosquito breeding sites and abundance using an unmanned aircraft," *Journal of the American Mosquito Control Association*, vol. 35, no. 3, pp. 228–232, Aug. 2019.
- [21] D. T. Bravo, G. A. Lima, W. A. L. Alves, V. P. Colombo, L. Djogbénou, S. V. D. Pamboukian, C. C. Quaresma, and S. A. de Araujo, "Automatic detection of potential mosquito breeding sites from aerial images acquired by unmanned aerial vehicles," *Computers, Environment and Urban Systems*, vol. 90, no. 9, pp. 1–13, Nov. 2021.
- [22] DJI, "Phantom 4 Pro Specifications," <https://www.dji.com/phantom-4-pro>, accessed: 2021-09-02.
- [23] Z. Zhang, "A flexible new technique for camera calibration," *IEEE Transactions on Pattern Analysis and Machine Intelligence*, vol. 22, no. 11, pp. 1330–1334, Nov. 2000.
- [24] B. Sekachev, N. Manovich, M. Zhiltsov, A. Zhavoronkov, and D. Kalinin, "opencv/cvat v1.1.0," <http://doi.org/10.5281/zenodo.4009388>, 2020, accessed: 2021-09-01.
- [25] "Mosquito breeding grounds (MBG) database," <http://www.smt.ufrj.br/~tvdigital/database/mosquito>, 2021, accessed: 2021-09-20.
- [26] Z. Zhao, P. Zheng, S. Xu, and X. Wu, "Object detection with deep learning: A review," *IEEE Transactions on Neural Networks and Learning Systems*, vol. 30, no. 11, pp. 3212–3232, Jan. 2019.
- [27] K. He, X. Zhang, S. Ren, and J. Sun, "Deep residual learning for image recognition," in *IEEE Conference on Computer Vision and Pattern Recognition*, Las Vegas, USA, Jun. 2016, pp. 770–778.
- [28] T.-Y. Lin, P. Dollar, R. Girshick, K. He, B. Hariharan, and S. Belongie, "Feature pyramid networks for object detection," in *IEEE Conference on Computer Vision and Pattern Recognition*, Honolulu, USA, Jul. 2017, pp. 936–944.
- [29] W. Han, P. Khorrami, T. L. Paine, P. Ramachandran, M. Babaeizadeh, H. Shi, J. Li, S. Yan, and T. S. Huang, "Seq-NMS for video object detection," *arXiv preprint arXiv:1602.08465*, 2016.
- [30] K. Kang, H. Li, J. Yan, X. Zeng, B. Yang, T. Xiao, C. Zhang, Z. Wang, R. Wang, X. Wang, and W. Ouyang, "T-CNN: Tubelets with convolutional neural networks for object detection from videos," *IEEE Transactions on Circuits and Systems for Video Technology*, vol. 28, no. 10, pp. 2896–2907, 2018.
- [31] T. Belhassen, H. Zhang, V. Fresse, and E.-B. Bourennane, "Improving video object detection by seq-bbox matching," in *International Joint Conference on Computer Vision, Imaging and Computer Graphics Theory and Applications*, Prague, Czech Republic, Feb. 2019, pp. 226–233.
- [32] A. Sabater, L. Montesano, and A. C. Murillo, "Robust and efficient post-processing for video object detection," in *IEEE/RISJ International Conference on Intelligent Robots and Systems*, Las Vegas, USA, Oct. 2020, pp. 10 536–10 542.
- [33] R. Padilla, W. L. Passos, T. L. B. Dias, S. L. Netto, and E. A. B. da Silva, "A comparative analysis of object detection metrics with a companion open-source toolkit," *Electronics*, vol. 10, no. 3, p. 279, Jan. 2021.
- [34] C. M. Bishop, *Pattern Recognition and Machine Learning*. New York, NY, USA: Springer, 2006.
- [35] Y. Wu, A. Kirillov, F. Massa, W.-Y. Lo, and R. Girshick, "Detectron2," <https://github.com/facebookresearch/detectron2>, 2019, accessed: 2021-08-15.